Supporting Information

Iridium coating Co nanoparticles embedded into highly porous N-doped carbon nanocubes grafted with carbon nanotubes as catalytic cathode for high-performance Li–O_2 battery

*Huixiang Yin [a, †], Dongdong Li [a, †], Zhenzhen Chi [a, †], Qian Zhang [a], Xiaoqiang Liu [a], Ling Ding [a], Shaoxiang Li [b], Jie Liu [d], Ziyang Guo [a, c, *], Lei Wang [a, b, *]*

a. Key Laboratory of Eco-chemical Engineering, Taishan Scholar Advantage and Characteristic Discipline Team of Eco-Chemical Process and Technology, College of Chemistry and Molecular Engineering, Qingdao University of Science and Technology, Qingdao 266042, China.

b. College of Environment and Safety Engineering, Qingdao University of Science and Technology, Qingdao, Shandong 266042, China.

c. Key Laboratory of Advanced Energy Materials Chemistry (Ministry of Education), College of Chemistry, Nankai University, Tianjin 300071, China.

d. College of Chemical Engineering, Qingdao University of Science and Technology, Qingdao 266042, China.

---

* Corresponding author. Tel & Fax: 0086-0532-84023409

E-mail address*: zyguo@qust.edu.cn; inorchemwl@126.com*

†These authors contributed equally to this work (Huixiang Yin, Dongdong Li and Zhenzhen Chi).

Material Preparation

Materials

Tetraethylene glycol dimethyl ether (TEGDME, 99.9 %) and LiTFSI (Sigma-Aldrich, 99.95 %) were purchased from Sigma-Aldrich Corporation. Cobalt nitrate hexahydrate ($Co(NO_3)_2 \cdot 6H_2O$, 99 %) and Zinc nitrate hexahydrate ($Zn(NO_3)_2 \cdot 6H_2O$, 99 %) were purchased from MACKLIN Reagent Corporation. 2-methylimidazole (99 %) were purchased from J&K Scientific Reagent Corporation. Cetyltrimethy lammonium bromide (CTAB) was purchased from Tianjin BODI Reagent Corporation. $IrCl_3 \bullet xH_2O$ (35.0~42.0 % Ir basls) was purchased from Aladdin Corporation. All chemicals were used as received without further purification.

Synthesis of Co-ZIFs and Co-NC preparation. Firstly, 4.1 g 2-methylimidazole was dissolved in 70 mL deionized water to form solution A. Additionally, 232.8 mg $Co(NO_3)_2 \cdot 6H_2O$ and 1 mg cetyltrimethylammonium bromide (CTAB) were added into 10 mL deionized water to form solution B. Then, solution B was quickly added to solution A and the mixture solution was continually stirred for 30 minutes. After that, the above solution was kept at room temperature for 24 hours. The precipitate was obtained by centrifugation and washed with ethanol several times. Finally, the resulting purple product was dried in a vacuum drying oven at 80 °C for further use. The obtained Co-ZIFs powder was heated to 900 °C with a rate of 5 $°C \cdot min^{-1}$ and kept at 900 °C for 2 h in the N_2 atmosphere.

Preparation for the Li_2O_2-Ir-Co/HP-NC/CNT or Li_2O_2-KB cathode for in situ DEMS test. Firstly, the as-prepared Ir-Co/HP-NC/CNT and Li_2O_2 powders were uniformly mixed with polytetrafluoroethylene (PTFE, 10%) solution in a mass ratio of 9:3:1. Next, the mixture was dispersed in the isopropanol. After that, the obtained material was rolled to form film and pressed on nickel net with a diameter of 12 mm. Finally, the Li_2O_2-Ir-Co/HP-NC/CNT cathode was assembled with Li anode in home-made battery for *in situ* DEMS test. What's more, the Li_2O_2-KB cathodes were prepared by the same method.

Computational method. Density functional theory (DFT) calculations were performed using the Vienna ab initio simulation package VASP (ref. S1). The exchange-correlation functional of Perdew-Burke-Ernzerhof (PBE) was used (ref. S2). The structure of Ir-Co/HP-NC/CNT and Co/HP-NC/CNT were modeled based on the structure of graphene and with 4 × 4 × 1 supercell. A vacuum size of 20 Å was employed to avoid interaction between periodic images. A *k*-point mesh of 2 × 2 × 1 and cutoff energy of 500 eV were applied for all the calculations. Both unit cell size and atom coordinates were optimized with a force convergence criterion of 0.001 eV $Å^{-1}$.

The adsorption energy (E_{ads}) of LiO_2/Li_2O_2 on Ir-Co/HP-NC/CNT or Co/HP-NC/CNT are calculated by:

$E_{ads} = E_{LiO_2/Li_2O_2@substrate}$-($E_{LiO_2/Li_2O_2}$+$E_{substrate}$),

where E_{LiO_2/Li_2O_2}, $E_{substrate}$, and $E_{LiO_2/Li_2O_2@substrate}$ are the total energy of LiO_2/Li_2O_2 molecular, clean Ir-Co/HP-NC/CNT or Co/HP-NC/CNT, and LiO_2/Li_2O_2 adsorbed on Ir-Co/HP-NC/CNT or Co/HP-NC/CNT, respectively.

The reaction free energy ΔG is calculated by the equation:

$\Delta G = \Delta E + \Delta ZPE - T\Delta S - qU$

Where ΔE is the total energy difference between products and reactants in each subreaction step obtained from the DFT calculations; ΔZPE and ΔS are the change of zero-point energy and entropy, respectively during the reaction processes; q and U are the charge transfer and the applied potential, respectively.

Characterization instrumentation

XRD measurements were performed on a Bruker D8 Advance. Field emission scanning electron microscopy SEM investigations were conducted using a JSM-6390 microscope from JEOL. Transmission electron microscopy (TEM) experiments were conducted using a JEOL 2011 microscope (Japan) operated at 200 kV. The Differential Electrochemical Mass Spectrometer measurement (Prisma Plus) was provided by Linglu Instruments (Shanghai) Co. Specific surface areas were calculated

by the Brunaure–Emmert–Teller method. Pore volumes and sizes were estimated from the pore-size distribution curves from the adsorption isotherms using the Barrett–Joyner–Halenda method. X-ray photoelectron spectroscopy (XPS) was conducted with a Thermo Escalab 250 equipped with a hemispherical analyzer and using an aluminum anode as a source. Fourier transform-infrared spectroscopy (FT-IR) tests were performed on a Nicolet 6700 spectrometer. LAND cycler (Wuhan Land Electronic Co. Ltd) was employed for electrochemical tests.

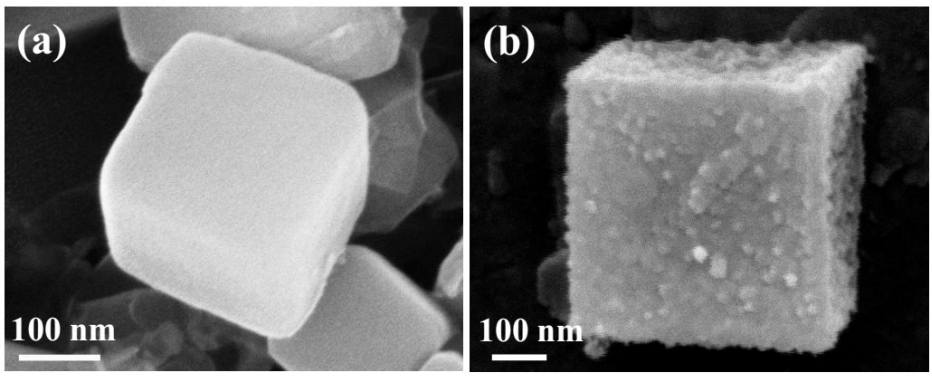

Figure S1 (a) SEM images of Co-ZIFs and (b) Co-NC

As shown in **Figure S1**, after the pyrolysis process, the Co-NC catalyst remains the typical nanocube structure which is similar to its precursor of Co-ZIFs.

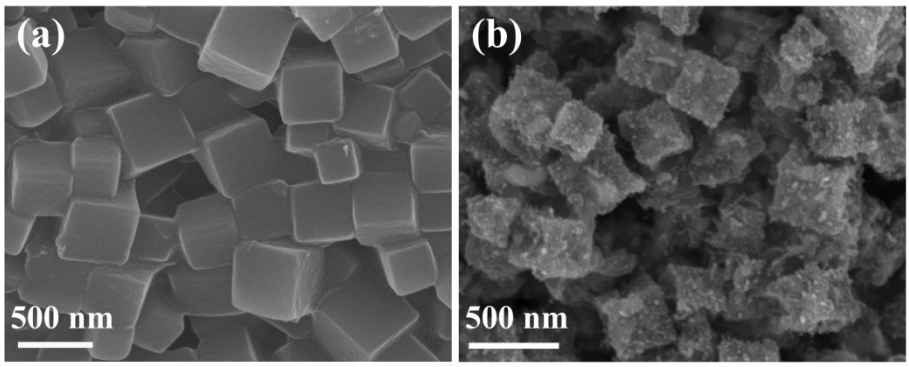

Figure S2 SEM images of (a) Co/Zn-ZIFs and (b) Ir-Co/HP-NC/CNT with low-magnifications.

As shown in **Figure S2**, Co/Zn-ZIFs show the typical 3D cubic structure with the smooth surface. After the pyrolysis process and Ir-coating, and Ir-Co/HP-NC/CNT catalyst remain the typical nanocube structure which is similar to its precursor.

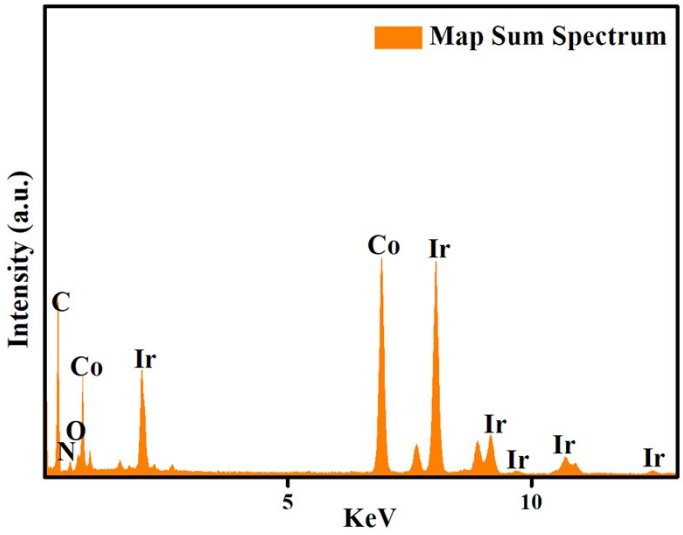

Figure S3 Energy-dispersive X-ray (EDX) result of Ir-Co/HP-NC/CNT.

It can be observed from **Figure S3** that C, N, Co and Ir elements are evenly distributed in Ir-Co/HP-NC/CNT.

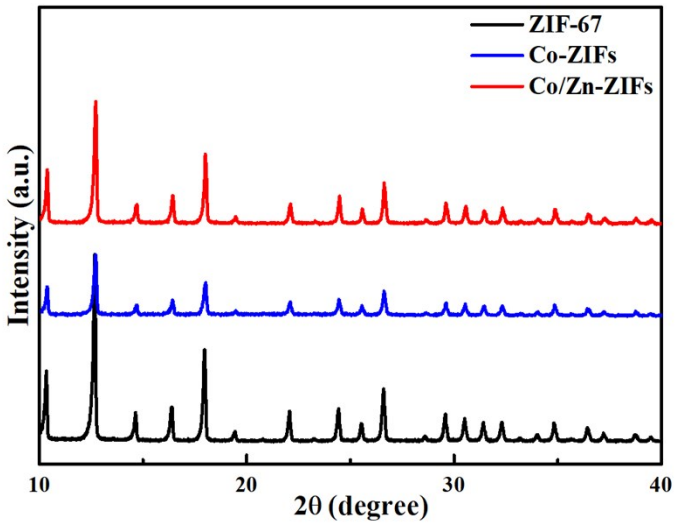

Figure S4 XRD patterns of ZIF-67, Co-ZIFs and Co/Zn-ZIFs.

As shown in **Figure S4**, the XRD diffraction peaks of Co-ZIFs and Co/Zn-ZIFs are coincident with the standard ZIF-67, which reveals Co-ZIFs and Co/Zn-ZIFs are synthesized successfully.

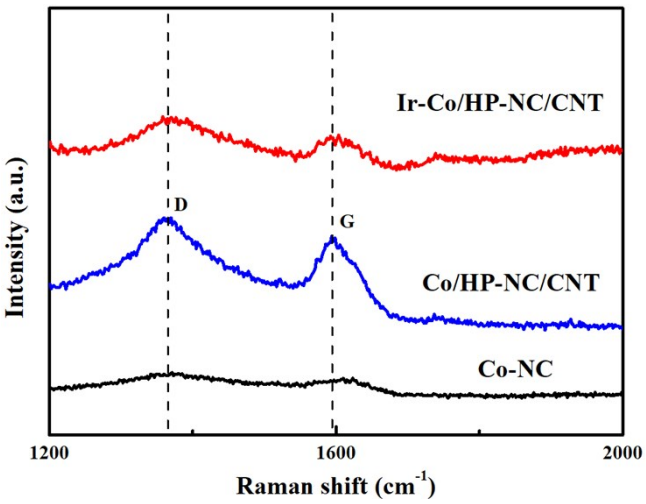

Figure S5 Raman spectra of Co-NC, Co/HP-NC/CNT and Ir-Co/HP-NC/CNT.

As shown in **Figure S5**, two prominent peaks at around 1363 cm^{-1} (D band) and 1593 cm^{-1} (G band) can be clearly observed in the Raman spectra of Co-NC, Co/HP-NC/CNT and Ir-Co/HP-NC/CNT, which confirms the co-existence of graphitized and defected carbon in these derivatives.

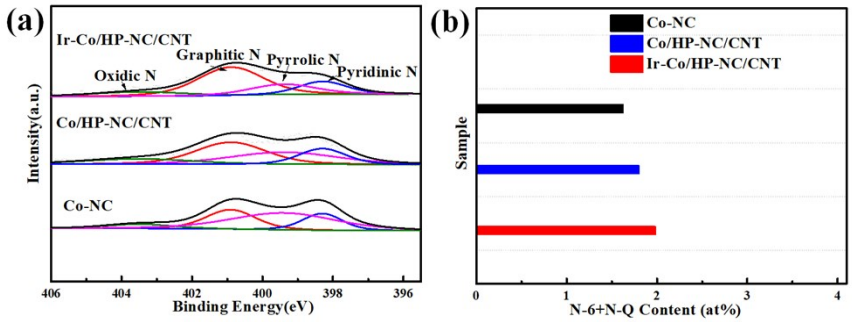

Figure S6 (a) High-resolution N 1s spectra of Co-NC, Co/HP-NC/CNT and Ir-Co/HP-NC/CNT. (b) The content percentages of pyridinic N (N-6) and graphitic N (N-Q) species calculated from the N 1s spectra for Co-NC, Co/HP-NC/CNT and Ir-Co/HP-NC/CNT.

The high-resolution N 1s XPS spectra of the three annealed derivatives have been deconvoluted into four peaks (**Figure S6a**): pyridinic N (N-6, ~398.3 eV), pyrrolic N (N-5, ~399.4 eV), graphitic N (N-Q, ~400.9 eV) and oxidic N (N-O, ~403.5 eV). Recent reports have demonstrated that N-6 and N-Q species are beneficial to ORR activity (ref. S3 and S4). **Figure S6** shows that the surface atom contents of the (N-6 + N-Q) phases in Ir-Co/HP-NC/CNT is higher than Co-NC or or Co/HP-NC/CNT. This phenomenon demonstrates that Ir-Co/HP-NC/CNT should a high ORR performance.

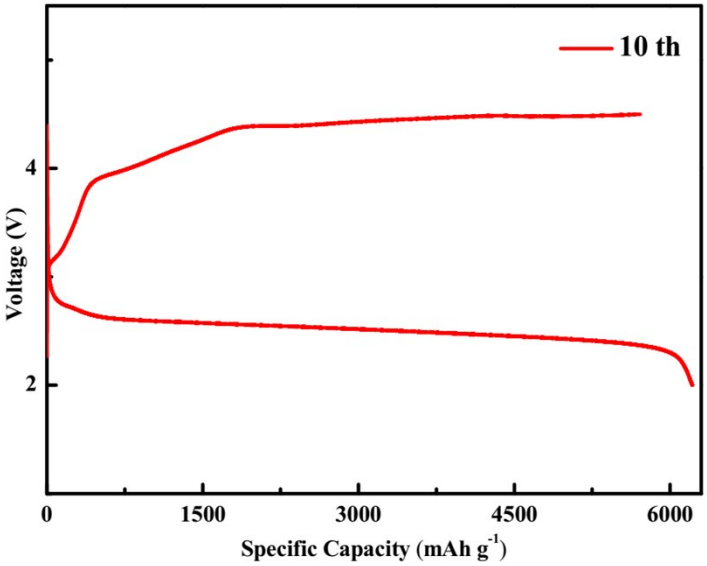

Figure S7 Discharge/charge profiles of the Li–O_2 battery with Ir-Co/HP-NC/CNT cathode after 10 full discharge/charge cycles at 500 mA g^{-1}.

As shown in **Figure S7**, the discharge and charge capacity of the Li–O_2 battery with Ir-Co/HP-NC/CNT cathode still remains 6215 mAh g^{-1} after 10 cycles, indicating the good capacity retention of Ir-Co/HP-NC/CNT electrode.

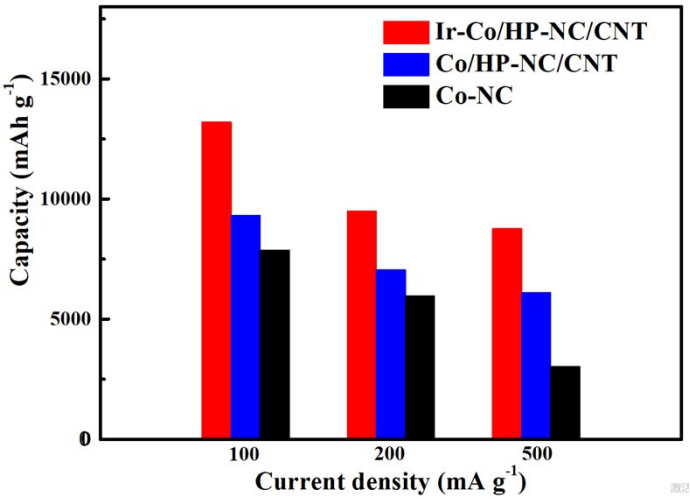

Figure S8 Discharge capacities of the Li–O_2 batteries with Co-NC, Co/HP-NC/CNT and Ir-Co/HP-NC/CNT cathodes at 100, 200 and 500 mA g^{-1}, respectively.

As shown in **Figure S8**, the Ir-Co/HP-NC/CNT-based Li–O_2 battery displays a discharge specific capacity of 13202 mAh g^{-1}, which is higher than those of Co/HP-NC/CNT (9308 mAh g^{-1}) and Co-NC (7880 mAh g^{-1}) based Li–O_2 cells. Even at a high current density of 200 or 500 mA g^{-1}, the Li–O_2 battery with Ir-Co/HP-NC/CNT still shows the best discharge capacity among the three air catalysts.

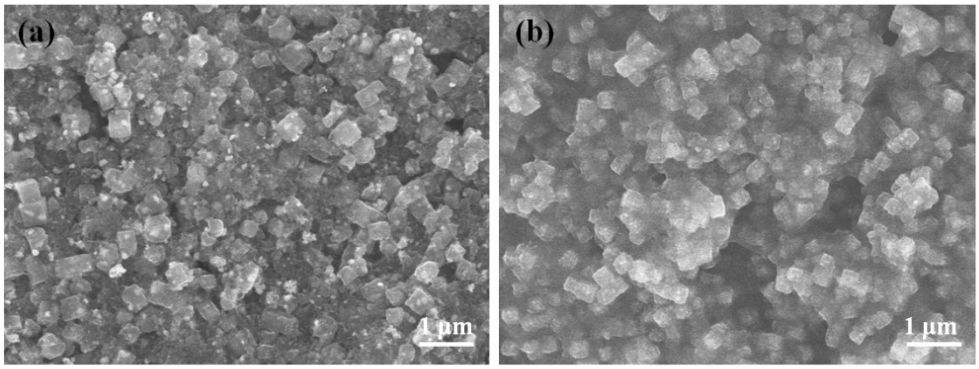

Figure S9 The SEM images of Ir-Co/HP-NC/CNT cathode (a) before and (b) after 25 cycles.

Compared with the pristine Ir-Co/HP-NC/CNT cathode (**Figure S9a**), Ir-Co/HP-NC/CNT in the cycled cathode can still maintain clear cube shape (**Figure S9b**). Moreover, the surface morphology of the Ir-Co/HP-NC/CNT cathode after 25 cycles (~corresponding to 100 h) is also similar to that of the Ir-Co/HP-NC/CNT electrode before cycling, except for only a small amount of discharge products coated on its surface (**Figure S9**). These results demonstrate that the Ir-Co/HP-NC/CNT cathode is very stable over cycling in Li–O_2 batteries.

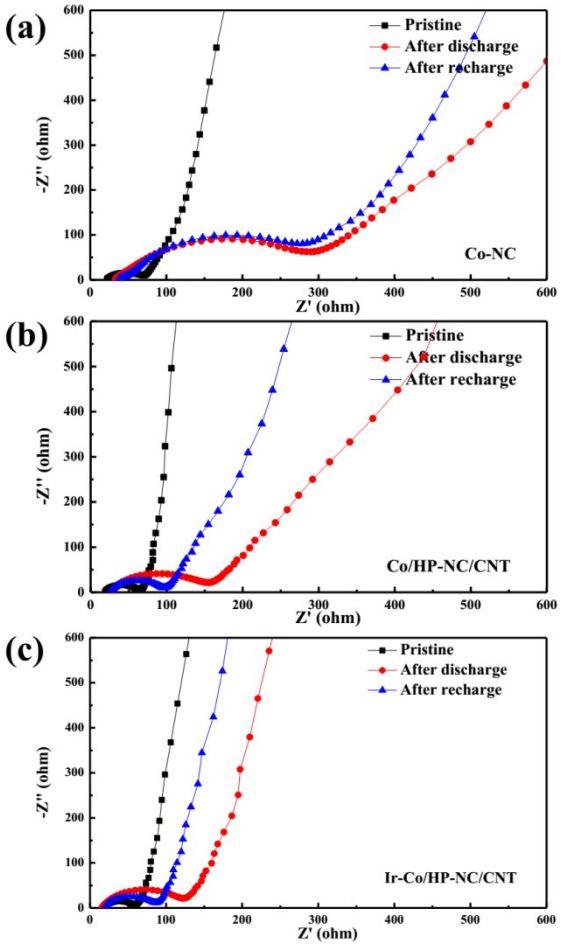

Figure S10 EIS spectra of Li–O_2 batteries using (a) Co-NC, (b) Co/HP-NC/CNT and (c) Ir-Co/HP-NC/CNT cathodes.

To further demonstrate the reversibility of catalysts, the Li–O_2 batteries with Ir-Co/HP-NC/CNT, Co/HP-NC/CNT or Co-NC cathodes are examined by Electrochemical Impedance Spectroscopy (EIS). It can be found from **Figure S10a** that the charge transfer resistance (R_{ct}) of the Li–O_2 battery with Co-NC cathode increases drastically from 70 to about 290 Ω after discharging, which can be attributed to the accumulation of the insoluble discharged products on the surface of electrode. After charging, the R_{ct} of Co-NC based Li–O_2 battery still remains 279 Ω, indicating that there are still the amounts of residual discharge products on O_2 electrode. In contrast, the Co/HP-NC/CNT or Ir-Co/HP-NC/CNT based Li–O_2 batteries exhibit better reversibility since they show the moderate impedance changes over cycling (**Figure S10b and c)**.

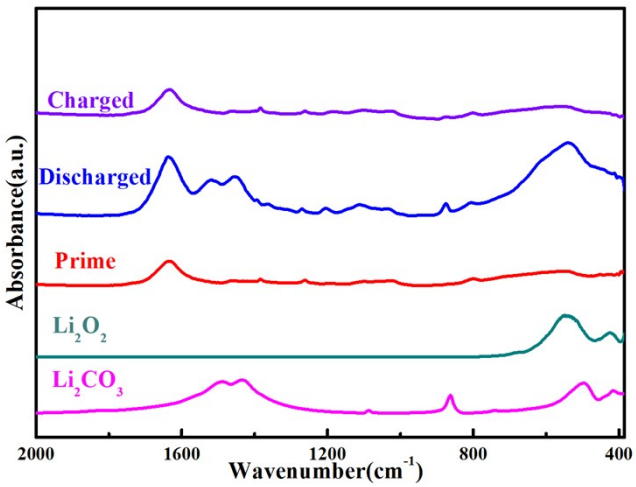

Figure S11 *Ex situ* FT-IR spectra of the pristine, discharged and charged Ir-Co/HP-NC/CNT based electrodes.

To further demonstrate the good reversibility of Ir-Co/HP-NC/CNT in Li–O_2 batteries, the *ex situ* FT-IR technology is applied to study the chemical composition changes of the Ir-Co/HP-NC/CNT cathodes during cycles. The FT-IR results of the Ir-Co/HP-NC/CNT cathodes under different discharge-charge conditions shown in **Figure S11** also confirm the reversible formation/decomposition of Li_2O_2 in Li–O_2 cells. Apart from Li_2O_2, the small amount of Li_2CO_3 also is formed on the discharged cathode and decomposed on the recharge cathode. It can be found that the XRD technology just can detect the crystalline materials and cannot find the less crystalline materials (ref. S5-7). The absence of the Li_2CO_3 peaks in the XRD patterns of the discharged Ir-Co/HP-NC/CNT cathodes (**Figure 4h**) further demonstrates that the formed Li_2CO_3 is limited and amorphous.

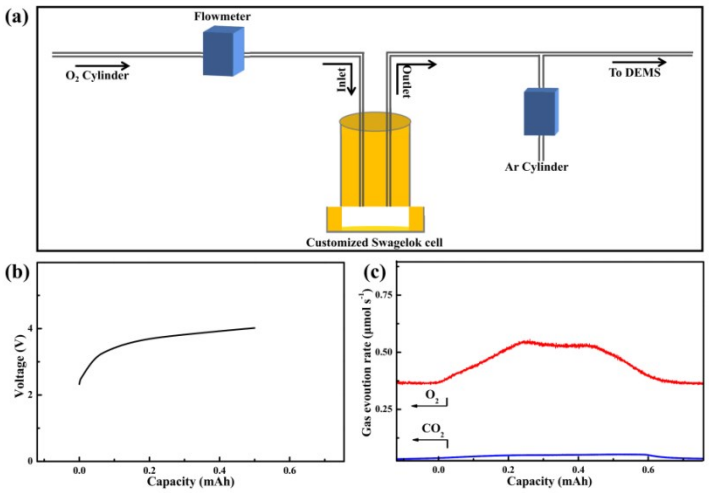

Figure S12 (a) Schematic illustration of the DEMS analysis system. (b) The charge profile of Li–O_2 battery using Ir-Co/HP-NC/CNT electrode and (c) the corresponding evolution curves of CO_2 and O_2 detected by *in situ* DEMS.

The DEMS system was built in-house and guided by the requirement to detect the gases evolved during the charge. A differential electrochemical mass spectrometer (Prisma Plus) with leak inlet is connected to a customized Swagelok cell assembly (**Figure S12a**). The cathode current collector is integrated with two tubes as purge gas inlet and outlet (**Figure S12a**). When analyzing the gas consumption over discharge process of Li–O_2 battery, the tested cell should be firstly discharged in the mixed gas of O_2 and Ar. When further analyzing the gas evolution over recharge process of Li–air battery, the system was purged with a pure Ar stream for 10 hours, and the background for O_2 and CO_2 was calibrated before the charge test and online gas analysis. Purge gas flows were typically 1 mL min^{-1}. **Figure S12b** and **c** present the gas evolution of the Ir-Co/HP-NC/CNT based Li–O_2 battery during recharge at a current of 0.3 mA. It can be clearly observed from **Figure S12c** that O_2 is the main generated gas upon recharging, indicating that Li_2O_2/O_2 conversion reaction dominates the charging process. Apart from the generated O_2, a very small amount of CO_2 evolved over charge, which can be attributed to the slight side reaction in Ir-Co/HP-NC/CNT based Li–O_2 cell. These results further confirm that Ir-Co/HP-

NC/CNT has high catalytic capacity and effectively improves the reversibility of Li–O_2 batteries.

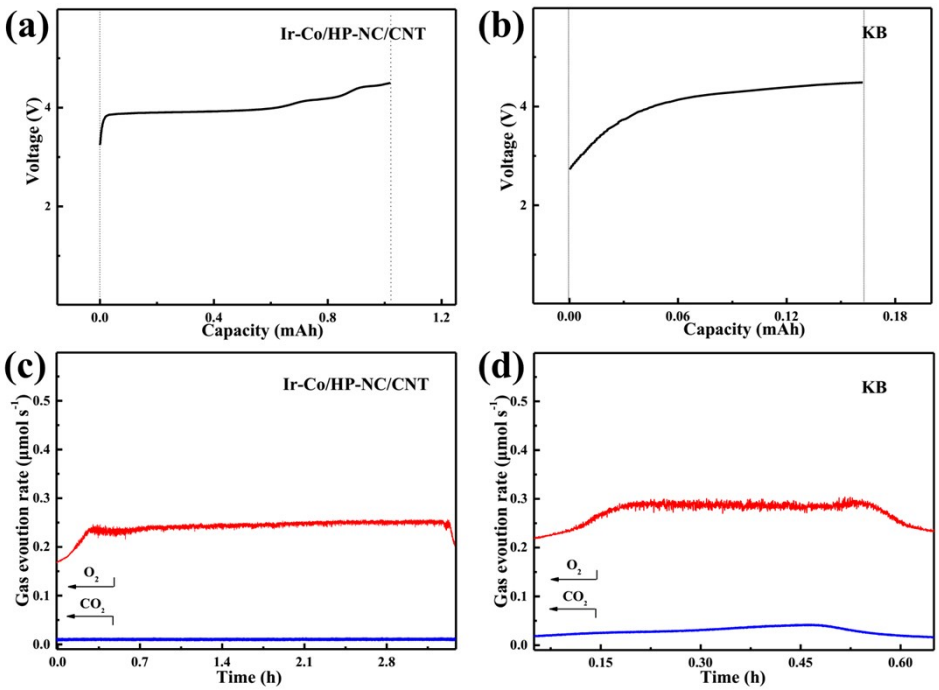

Figure S13 (a, b) Charge profiles and (c, d) the corresponding CO_2 and O_2 evolution curves detected by *in situ* DEMS of (a, c) Li_2O_2-Ir-Co/HP-NC/CNT cathode or (b, d) Li_2O_2-KB cathode.

As shown in **Figure S13a** and **b**, the charge overpotential of the Li_2O_2-KB cathode is obviously higher than that of the Li_2O_2-Ir-Co/HP-NC/CNT electrode. Moreover, there is only O_2 evolved over charge for the Li_2O_2-Ir-Co/HP-NC/CNT cathode (**Figure S13c**), but O_2 and CO_2 are generated at the same time on the Li_2O_2-KB electrode during charge. These results confirmthat the Ir-Co/HP-NC/CNT catalyst not only obviously reduce charge overpotential, but also inhibit side reactions over recharge.

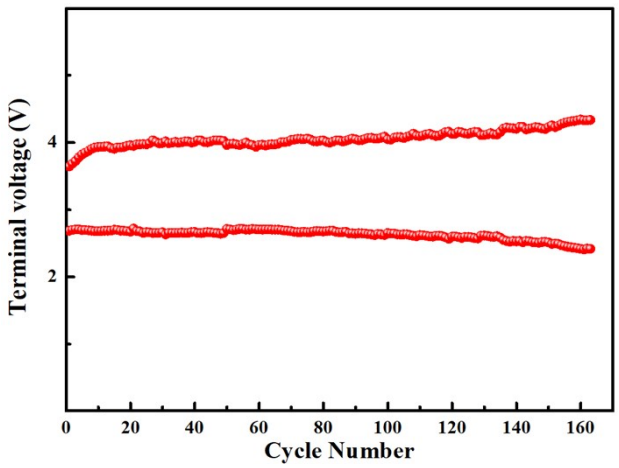

Figure S14 The discharge/charge terminal voltage variations over cycles of the Ir-Co/HP-NC/CNT based bulk-shaped Li–air cell.

As shown in **Figure S14**, the charge potentials of the Ir-Co/HP-NC/CNT based bulk-shaped Li–air cell are always lower than 4.1V during 120 cycles, which further highlights the superiority of Ir-Co/HP-NC/CNT on catalyzing the reactions in Li–air batteries.

Table S1 ICP-OES analysis results

Sample	Co/wt%	Ir/wt%
Ir-Co/HP-NC/CNT	26.35%	4.15%

As shown in **Table S1**, the contents of Co and Ir element in Ir-Co/HP-NC/CNT are 26.35 and 4.15 wt%, respectively.

Table S2 The pore volume of Co-NC, Co/HP-NC/CNT and Ir-Co/HP-NC/CNT.

Sample	pore volume ($cm^3 \cdot g^{-1}$)
Co-NC	0.237
Co/HP-NC/CNT	0.311
Ir-Co/HP-NC/CNT	0.349

As shown in **Table S2**, the pore volume of Co/HP-NC/CNT and Ir-Co/HP-NC/CNT are much larger than that of Co-NC, which should be attributed to the additional pores derived from the evaporation of Zn at high temperature.

Table S3 Summary of the specific capacity of various cathode catalysts.

Cathode material	Current ($mA\ g^{-1}$)	Specific Capacity ($mAh\ g^{-1}$)	Reference
Co@PNCS	200	6725	8
Ag@LFO	100	8476	9
CNT@Ni@NiCo	150	10046	10
Co[Co, Fe]O_4/NG	100	12000	11
GDP-Mo_2C@NCF	100	7437	12
Co-N-CNT/CNF	100	11512	13
Ir-Co/HP-NC/CNT	**100**	**13200**	**This work**

As listed in **Table S3**, the Ir-Co/HP-NC/CNT-based Li–O_2 battery delivered a discharge capacity of 13200 mAh g^{-1} at 100 mA g^{-1}, which is better than many recently reported catalysts (ref. S8-13).

Table S4 Summary of cycle performance under 1000 mAh g^{-1} of various cathode catalysts.

Cathode material	Cycle Capacity/Current (mAh g^{-1}/mA g^{-1})	Cycle Performance	Reference
Co[Co, Fe]O_4/NG	1000/100	110	11
GDP-Mo_2C@NCF	1000/100	105	12
MMC-50	1000/500	56	14
CCO@rGO	1000/200	105	15
TiO_{2-x} nanoboxes	1000/200	200	16
Co_4N/CNF	1000/200	100	17
V_{Se}-$CoSe_2$@N-CC	1000/200	134	18
Co_3O_4@Co_3O_4/Ag	1000/200	80	19
Ag-MnO_2	1000/400	170	20
Ir@DHG	1000/2000	150	21
Ir-Co/HP-NC/CNT	**1000/500**	**320**	**This work**

As listed in **Table S4**, the cycling stability of the Li–O_2 battery using Ir-Co/HP-NC/CNT cathode in our work is much higher than most of the recent reported Li–O_2 batteries (ref. S11, S12 and S14-21).

Refereen

ref. S1: E. Blöchl, *Phys. Rev. B*, 1994, 50, 17953–17979.

ref. S2: J. P. Perdew, K. Burke and M. Ernzerhof, *Phys. Rev. Lett.*, 1996, 77, 3865–3868.

ref. S3: Z. D. Yang, X. Y. Yang, T. Liu, Z.W. Chang, Y. B. Yin, X. B. Zhang, J. M. Yan, Q. Jiang, *Small*, 2018, 14, 1800590.

ref. S4: G. N. Zhang, L. Zhang, S. Q. Zhao, S. G. Lu, Y. Lu, H. B. Sun, L. Wang, *RSC Adv.*, 2020, 10, 3853–3860.

ref. S5: J. X. Li, L. Chen, R. L. Ye, J. G. Gao, W. J. Huang, Y. B. Lin, Z. G. Huang, *Appl. Surf. Sci.*, 2020, 507, 145103.

ref. S6: Y. J. Yun, H. Park, J. K. Kim, S. Unithrattil, H. T. Huu, D. W. Kim, S. S. Lee, Y. Kang, W. B. Im and S. Choi, *J Electrochem Soc* 2020, 167, 080537.

ref. S7: A. Kondori, Z. Jiang, M. Esmaeilirad, M. T. Saray, A. Kakekhani, K. Kucuk, P. N. M. Delgado, S. Maghsoudipour, J. Hayes, C. S. Johnson, C. U. Segre, R. S. Yassar, A. M. Rappe, M. Asadi., *Adv. Mater.* 2020, 32, 2004028.

ref. S8: Y. Zhai, J. Wang, Q. Gao, Y. Fan, C. Hou, Y. Hou, H. Liu, Q. Shao, S. Wu, L. Zhao, T. Ding, F. Dang, Z. Guo, *Journal of Catalysis*, 2019, 377, 534–542.

ref. S9: D. Q. Cao, Q. Z. Wang, X. Yin, Y. D. Sun, M. Ma, Y. P. Wu, X. J. Liu, *Energy Fuels*, 2020, 34, 10225−10231.

ref. S10: Z. Li, J, Yang, D. A. Agyeman, M. Park, W. Tamakloe, Y. Yamauchicd, Y. M. Kang, *J. Mater. Chem. A*, 2018, 6, 10447–10455.

ref. S11: Y. D. Gong, W. Ding, Z. P. Li, R. Su, X. L. Zhang, J. Wang, J. G. Zhou, Z. W. Wang, Y. H. Gao, S. Q. Li, P. F. Guan, Z. D. Wei and C. W. Sun, *ACS Catal.*, 2018, 8, 4082–4090.

ref. S12: X. Z. Ren, M. J. Huang, S. Luo, Y. L. Li, L. B. Deng, H. W. Mi, L. N. Sun and P. X. Zhang, *J. Mater. Chem. A*, 2018, 6, 10856–10867.

ref. S13: Z. D. Yang, X. Y. Yang, T. Liu, Z. W. Chang, Y. B. Yin, X. B. Zhang, J. M. Yan, Q. Jiang, *Small*, 2018, 14, 1800590.

ref. S14: D. Y. Kim, X. Jin, C. H. Lee, D. W. Kim, J. D. Suk, J. K. Shon, J. M. Kim, Y. K. Kang, *Carbon*, 2018, 133, 118–126.

ref. S15: J. D. Liu, Y. Y. Zhao, C. G. Wang, G. H. Yue and Q. Chen, *Nano-Micro Lett.*, 2018, 10, 22.

ref. S16: G. X. Liu, W. Li, R. Bi, C. A. Etogo, X. Y. Yu and L. Zhang, *ACS Catal.*, 2018, 8, 1720–1727.

ref. S17: K. R. Yoon, K. Shin, J. Park, S. H. Cho, C. Kim, J. W. Jung, J. Y. Cheong, H. R. Byon, H. M. Lee and I. D. Kim, *ACS Nano*, 2018,12, 128–139.

Ref. S18: Z. W. Li, J. H. Yang, D. A. Agyeman, M. Park, W. Tamakloe, Y. Yamauchi, Y. M. Kang, *J. Mater. Chem. A*, 2018, 6, 10447–10455.

ref. S19: R. Gao, Z. Z. Yang, L. R. Zheng, L. Gu, L. Liu, Y. L. Lee, Z. B. Hu and X. L. Liu, *ACS Catal.*, 2018, 8, 1955–1963.

ref. S20: L. N. Dai, Q. Sun, L. N. Chen, H. H. Guo, X. K. Nie, J. Cheng, J. G. Guo, J. W. Li, J. Lou, L. J. Ci, *Nano Res.*, 2020, 13, 2356–2364.

ref. S21: W. Zhou, Y. Cheng, X. F. Yang, B. S. Wu, H. J. Nie, H. Z. Zhang and H. M. Zhang, *J. Mater. Chem. A*, 2015, 3, 14556–14561.